High compressibility of synthetic analogous of binary iridium–ruthenium and ternary iridium–osmium–ruthenium minerals

Kirill V. Yusenko,[a*] Svetlana A. Martynova,[b,c] Saiana Khandarkhaeva,[d] Timofey Fedotenko,[e] Konstantin Glazyrin,[f] Egor Koemets,[d] Maxim Bykov,[d] Michael Hanfland,[g] Konrad Siemensmeyer,[h] Alevtina Smekhova,[i] Sergey A. Gromilov,[b,c] Leonid S. Dubrovinsky[d]

[a]BAM Federal Institute for Materials Research and Testing, Richard-Willstätter-Str. 11, 12489 Berlin, Germany

[b]Nikolaev Institute of Inorganic Chemistry, Lavrentiev Ave. 3, 630090 Novosibirsk, Russia

[c]Novosibirsk State University, Pirogova str. 2, 630090 Novosibirsk, Russia

[d]Bayerisches Geoinstitut, University of Bayreuth, 95440 Bayreuth, Germany

[e]Material Physics and Technology at Extreme Conditions, Laboratory of Crystallography, University of Bayreuth, D-95440 Bayreuth, Germany

[f]Photon Sciences, Deutsches Elektronen-Synchrotron, Notkestr. 85, 22607 Hamburg, Germany

[g]ESRF – The European Synchrotron, 71 Av. des Martyrs, 38000, Grenoble, France

[h]Helmholtz-Zentrum Berlin für Materialien und Energie, Hahn-Meitner-Platz 1, 14109 Berlin, Germany

[i]Helmholtz-Zentrum Berlin für Materialien und Energie, Albert-Einstein-Str. 15, 12489 Berlin, Germany

*Corresponding author: BAM Federal Institute for Materials Research and Testing, Richard-Willstätter-Str. 11, 12489 Berlin, Germany; kirill.yusenko@bam.de

Abstract

Hcp–$Ir_{0.24}Ru_{0.36}Os_{0.40}$ and *fcc*–$Ir_{0.84}Ru_{0.06}Os_{0.10}$ ternary alloys as well as binary *hcp*–$Ir_{0.33}Ru_{0.67}$ and *fcc*–$Ir_{0.75}Ru_{0.25}$ ones were prepared using thermal decomposition of $[Ir_xRu_{1-x}(NH_3)_5Cl][Os_yIr_{(1-y)}Cl_6]$ single-source precursors in hydrogen flow below 1070 K. These single-phase alloys correspond to ternary and binary peritectic phase diagrams and can be used as synthetic models for rare iridosmine minerals. Thermal decomposition of parent bimetallic precursor $[Ir(NH_3)_5Cl][OsCl_6]$ has been investigated using *in situ* powder X-ray diffraction in inert and reductive atmospheres. In reductive atmosphere, $[Ir(NH_3)_5Cl][OsCl_6]$ forms $(NH_4)_2[OsCl_6]$ as crystalline intermediate; Ir from its cationic part is reduced by hydrogen with a formation of defect *fcc*-structured metallic particles; the final product is a metastable *hcp*–$Ir_{0.5}Os_{0.5}$ alloy. In inert atmosphere, the salt decomposes at higher temperature without a formation of any detectable crystalline intermediates; two-phase *fcc*+*hcp* mixture forms directly above 800 K. Room temperature compressibility up to 50 GPa has been studied for all prepared alloys in diamond anvil cells. Investigated ternary and binary alloys do not show any phase transitions upon compression at room temperature. In contrast with other investigated ultra-incompressible refractory alloys with osmium and iridium, *hcp*–$Ir_{0.33}Ru_{0.67}$, *fcc*–$Ir_{0.75}Ru_{0.25}$ binary and *fcc*–$Ir_{0.84}Ru_{0.06}Os_{0.10}$ ternary alloys show higher compressibility in comparison with pure metals. *Fcc*–$Ir_{0.75}Ru_{0.25}$ alloy shows several magnetic phase transitions (at approx. 3.4 K, 135 K and 233 K) that could be related to different magnetic phases.

Keywords: iridosmine, refractory alloys, single-source precursors, high-pressure high-temperature.

1. Introduction

Refractory alloys based on platinum group metals have found broad applications as materials for extreme environments. Platinum group binary and ternary alloys are highly stable under mechanical impact, oxidative environment as well as under heating and compression [1]. Since their discovery, platinum group metallic minerals such as ferroplatinum and iridosmine were considered as one of the most important sources for rare platinum group metals [2]. Such minerals generally containing several components and having as minimum two phases are formed from the magmatic melt under high-pressure high-temperature conditions [3–5]. Iridosmine is an example of a unique metallic mineral with high hardness. Under ambient conditions, it has the highest density among all minerals and materials known. As soon as it is the main source of iridium and osmium its genesis and properties attract attention of geologists and geophysicists.

Iridosmine minerals are mainly Ir–Os–Ru ternary alloys. Ir–Os and Ir–Ru binary phase diagrams contain *fcc* and *hcp* stability fields which also exist in ternary Ir–Os–Ru phase diagram. Nevertheless, single-phase mineral samples are quite rare and have never been investigated to obtain fundamental properties of Ir–Os–Ru alloys while ternary Ir–Os–Ru phase diagram has never been investigated experimentally. High hardness and small particle sizes in multiphase iridosmine mineral probes do not give an experimental possibility to investigate individual phases using X-ray diffraction and obtain their precise cell parameters at ambient conditions as well as upon heating and compression. High melting temperature does not give much possibilities to probe experimentally fundamental properties of iridosmine minerals under realistic geological conditions.

After 1960, Cabri and Harris performed detailed systematic study of iridosmine minerals and drafted Ir–Os–Ru phase diagram based on the phase and elemental composition of existing natural multicomponent and multiphase samples [6]. Nevertheless, direct experimental knowledge about Ir–Os and Ir–Ru binary alloys as well as Ir–Os–Ru ternary systems might be

important for understanding a general constitution of ternary and multicomponent natural and synthetic alloys; stability, thermal expansion and pressure compressibility studies of binary and ternary alloys might give a solid basis for modelling of thermodynamic conditions of iridosmine mineral formation and transformation.

High-pressure properties of Ir–Os binary alloys were recently investigated up to 140 GPa [7, 8]. In contrast, binary Ir–Ru alloys as well as ternary Ir–Os–Ru alloys and a corresponding ternary phase diagram have never been investigated experimentally under heating and compression. However, ternary Ir–Os–Ru phase diagram contains three binary sides Os–Ru, Ir–Os and Ir–Ru, all of which were constructed experimentally. In the current study, we report synthesis, thermal expansion and high-pressure compressibility up to 50 GPa of *fcc*- and *hcp*-structured Ir–Ru binary and Ir–Os–Ru ternary alloys. The first magnetometry results of Ir–Ru binary alloys are also demonstrated. Refractory alloys were prepared in the form of single phases using thermal decomposition of single-source precursors. Binary Ir–Ru alloys were prepared from $[Ru(NH_3)_5Cl]_2[IrCl_6]Cl_2$ (*hcp*–$Ir_{0.33}Ru_{0.67}$) and $[Ir(NH_3)_5Cl]_{0.50}[Ru(NH_3)_5Cl]_{0.50}[IrCl_6]$ (*fcc*–$Ir_{0.75}Ru_{0.25}$) single-source precursors below 900 K in a hydrogen flow. Ternary Ir–Os–Ru alloys were obtained as products of thermal decomposition of $[Ir(NH_3)_5Cl]_a[Ru(NH_3)_5Cl]_{1-a}[IrCl_6]_b[OsCl_6]_{1-b}$ below 1100 K in a hydrogen flow as well.

2. Experimental

$[Ir(NH_3)_5Cl]Cl_2$ and $[Ru(NH_3)_5Cl]Cl_2$ were prepared from $IrCl_4{\cdot}xH_2O$ and $RuCl_3{\cdot}xH_2O$ [9, 10]; $(NH_4)_2[OsCl_6]$, $K_2[IrCl_6]$ and $(NH_4)_2[IrCl_6]$ were obtained from Sigma Aldrich. *Hcp*–$Ir_{0.33}Ru_{0.67}$ was prepared from an individual compound $[Ru(NH_3)_5Cl]_2[IrCl_6]Cl_2$, and *fcc*–$Ir_{0.75}Ru_{0.25}$ was prepared from $[Ir(NH_3)_5Cl]_{0.50}[Ru(NH_3)_5Cl]_{0.50}[IrCl_6]$ according to published protocols [11]. Briefly, for a preparation of $[Ru(NH_3)_5Cl]_2[IrCl_6]Cl_2$ a solution of $K_2[IrCl_6]$ in 0.1 M HCl was mixed with solid $[Ru(NH_3)_5Cl]Cl_2$ and kept in the dark for 5 days. After complete dissolution of starting $[Ru(NH_3)_5Cl]Cl_2$, dark brown crystals were filtered from the solution,

washed with water and acetone, and dried in air. $[Ir(NH_3)_5Cl]_{0.50}[Ru(NH_3)_5Cl]_{0.50}[IrCl_6]$ was prepared from water solution: calculated amounts (1:1 molar ratio) of $[Ir(NH_3)_5Cl]Cl_2$ and $[Ru(NH_3)_5Cl]Cl_2$ were dissolved in a minimum amount of water and mixed with a $K_2[IrCl_6]$ water solution. A dark brown precipitate was filtered after 3 h, washed with water and acetone, and dried in air. Precursors were heated in hydrogen flow up to 900 K, annealed for 30 minutes and cooled down to room temperature.

Ternary Ir–Os–Ru alloys were also prepared by thermal decomposition of single-source precursors (Table 1) [12]. Precursors were synthesised from water solutions according to the following procedure, where the amounts of $[Ir(NH_3)_5Cl]Cl_2$, $[Ru(NH_3)_5Cl]Cl_2$, $(NH_4)_2[OsCl_6]$ and $(NH_4)_2[IrCl_6]$ were calculated according to the general equation listed below. Mixtures of chloropentaammines and hexachlorometallates were separately dissolved in hot water. The hot solutions were mixed, stirred and naturally cooled down to room temperature. The brownish crystalline precipitates were filtered, washed with cold water and ethanol, and dried afterwards. Metallic alloys were prepared by thermal decomposition of precursor's powders in H_2 flow at 1070 K.

Morphology and compositions of alloys were analysed using a FEI Quanta 200 FEG-ESEM scanning-electron microscope equipped for energy dispersive X-ray spectroscopy (EDX). Final metallic alloys were sieved on two side glued conductive carbon tape as thin homogeneous layer of individual isolated particles. Such approach does not give systematic errors and has been tested on *hcp*–$Ir_{0.33}Ru_{0.67}$ binary alloy prepared from the discrete compound $[Ru(NH_3)_5Cl]_2[IrCl_6]Cl_2$ with known composition. Compositions were averaged in 4–5 points.

Phase composition and cell parameters of metallic alloys were obtained by powder X-ray diffraction (PXRD) using an ARL X'TRA diffractometer (Cu*K*α-radiation, Ni-filter, Bragg-Brentano reflection geometry, 2Θ = 5–100°, $\Delta 2\Theta$ = 0.03°, 10 s/step, room temperature). Polycrystalline samples were slightly ground with hexane using an agate mortar, and the resulting suspensions were deposited on a polished side of quartz sample holder; a smooth thin

layer was formed after drying. Silicon powder was taken as an external standard (a = 5.4309 Å, FWHM 2Θ = 0.1°) for calibration of the zero-shift of the goniometer and the instrumental line broadening. Only *fcc*- and *hcp*-structured alloys as well as their two-phase mixtures were found as products of thermal decomposition of single-source precursors (Table 1).

Ambient pressure thermal expansion curves for *hcp*–$Ir_{0.24}Ru_{0.36}Os_{0.40}$ and *fcc*–$Ir_{0.84}Ru_{0.06}Os_{0.10}$ alloys were obtained on the basis of the diffraction data collected at the I11 beamline at the DIAMOND Light Source (Oxfordshire, UK, λ = 0.825352 Å). The samples as fine powders were placed in 0.5-mm glass capillaries and cooled down to 100 K using Oxford cryo-stream device. Temperature-dependent diffraction patterns were collected upon temperature increase from 100 K to 400 K in 10 degrees steps using a Mythen-2 position sensitive detector [13]. Primary data for temperature dependence of cell parameters can be found in Supplementary Tables S4 and S6.

Thermal decomposition of $[Ir(NH_3)_5Cl][OsCl_6]$ in reductive atmosphere has been investigated *in situ* using powder X-ray diffraction (PXRD) set-up on the Swiss-Norwegian Beam Lines (BM01A, European Synchrotron Radiation Facility (ESRF), Grenoble, France). The sample, in a powder form, was placed in 0.5 mm fused quartz mark tube (Hilgenberg GmbH, Germany). The tube was connected to a 2 vol.% H_2/He flow (0.1-0.5 ml/min) and heated with a hot air stream from room temperature to 1000 K with a ramp rate of 10 K/min. Temperature has been calibrated by thermal expansion of silver powder cell parameters as an external standard. The wavelength (λ = 0.68894 Å) and sample-to-detector distance have been calibrated using a LaB_6 powder (NIST SRM 660c) as an external standard. Data have been collected every 20 s (approximately every 3 K in the temperature scale) using a PILATUS2M 2D flat detector. Thermal decomposition of $[Ir(NH_3)_5Cl][OsCl_6]$ in inert atmosphere has been investigated using a similar set up installed at the ID11 beamline (ESRF) in N_2 flow. The wavelength (λ = 0.30860 Å) and sample-to-detector distance have been calibrated using a CeO_2 powder as an external standard. Data have been collected every second (every 0.5 K in the temperature scale) using a

FReLoN 2K (ATMEL chip) flat detector. Experimental two-dimensional diffraction data have been converted and processed using the SNBL software toolbox [14]. Temperature dependent PXRD patterns were plotted and analysed using Powder3D software [15]. Phase compositions were verified using the PDF database [16].

Room temperature compressibility curves for *hcp*–$Ir_{0.33}Ru_{0.67}$ and *fcc*–$Ir_{0.75}Ru_{0.25}$ binary alloys were collected at ID15B beamline up to 46 GPa (ESRF, Grenoble; λ = 0.411235 Å, 250 μm culet sizes, He as a pressure transmitting medium, ruby as a pressure calibrant, MAR 555 flat panel detector, beam size 10(*v*)×10(*h*) μm^2). Compressibility curve for *hcp*–$Ir_{0.24}Ru_{0.36}Os_{0.40}$ ternary alloy was also collected at ID15B beamline up to 40 GPa (ESRF, λ = 0.411546 Å, 300 μm culet sizes, Ne as a pressure transmitting medium, ruby as a pressure calibrant, MAR 555 flat panel detector, beam size 10(*v*)×10(*h*) μm^2). The sample was loaded in diamond anvil cells (DAC) equipped with conically supported Boehler Almax anvils.

Compressibility curve for *fcc*–$Ir_{0.84}Ru_{0.06}Os_{0.10}$ ternary alloy was collected at high pressure beamline P02.2 (Petra III, DESY, Hamburg) (λ = 0.2917 Å, Perkin Elmer XRD1621 flat panel detector, beam size 5(v)×8(h) μm^2) up to 51 GPa. The sample was loaded in the BX90-type DAC [17] equipped with Boehler-Almax diamonds (250 um culet size). Neon was loaded at 1.5 kbar in Bayerisches Geoinstitut [18] and served as a pressure transmitted medium and an internal pressure calibrant. Additionally, a piece of Au was loaded as a pressure marker in the sample chamber. Pressure values were averaged with respect to both standards using the corresponding equations of state [19].

High-pressure diffraction data were integrated using DIOPTAS software [20]. The unit cell parameters, the background, and the line-profile parameters for the sample and Ne were refined simultaneously using JANA2006 software [21]. The P–V data were fitted using EoS–Fit7 software [22]. All primary data for pressure dependent cell parameters are summarized in Supplementary Tables S1–S3 and S5. Modelling of binary and ternary phase diagrams has been

performed using PANDAT 6 software [23]. Thermodynamic parameters for pure metals were taken from the SGTE database [24].

IR-spectra were collected using a Scimitar FTS 2000 Fourier-spectrometer «DIGILAB» (4000–400 cm^{-1}, medium IR region) and a Vertex 80 «Bruker» spectrometer (600–100 cm^{-1}, far IR region). Samples were pressed in dry KBr pellets for the medium IR region and in polyethylene pellets for the far IR region. Raman Spectra were collected using a LabRAM HR, Horiba spectrometer with Ar laser CVI Melles Griot (λ = 633 nm). Spectra were collected in reflection mode under Raman microscope with a 0.5 cm^{-1} resolution.

Conventional magnetometry measurements were carried out on *hcp*–$Ir_{0.33}Ru_{0.67}$ (9.12 mg) and *fcc*–$Ir_{0.75}Ru_{0.25}$ (8.66 mg) alloys using a Magnetic Properties Measurement System (MPMS, Quantum Design) in magnetic fields up to 7 T and in the temperature range of 2–360 K in the Bulk Properties Lab of the ”CoreLab Quantum Materials” at the Helmholtz-Zentrum Berlin (HZB). The samples in the powder form were placed in a standard plastic capsule; a slow field sweep rate was chosen to avoid slight movements of the powder grains during the measurements.

3. Results and discussion

3.1. Synthesis of binary and ternary alloys from single-source precursors

In previous studies, mainly individual single-source precursors for binary and multicomponent refractory alloys were investigated [25, 26]. Ternary and multicomponent alloys were prepared only sporadically for selected systems [12, 27]. In the current study, a single-source precursors strategy has been systematically applied for synthesis of ternary refractory alloys in a broad range of alloy’s compositions for the first time.

$[Ir(NH_3)_5Cl][OsCl_6]$ has been proposed as a precursor for *hcp*–$Ir_{0.5}Os_{0.5}$ and $[Ir(NH_3)_5Cl]_2[OsCl_6]Cl_2$ – for two-phase $Ir_{0.67}Os_{0.33}$ [25]; $[Ru(NH_3)_5Cl][IrCl_6]$ – for two-phase $Ir_{0.5}Ru_{0.5}$; $[Ru(NH_3)_5Cl]_2[IrCl_6]Cl_2$ – for single-phase *hcp*–$Ir_{0.33}Ru_{0.67}$ [10]; $[Ru(NH_3)_5Cl][OsCl_6]$ and $[Ru(NH_3)_5Cl]_2[OsCl_6]Cl_2$ – for *hcp*–$Os_{0.5}Ru_{0.5}$ and *hcp*–$Os_{0.33}Ru_{0.67}$, correspondingly [29]. It

also has been shown that isoformular compounds are isostructural and can be co-crystallized from water solutions. Such an important finding allowed us to prepare binary *fcc*- and *hcp*-structured Ir–Ru alloys in the whole range of compositions according to the following generalised chemical equilibria [10].

Crystallization from water solution: $x[Ir(NH_3)_5Cl]Cl_2 + (1\text{-}x)[RuNH_3)_5Cl]Cl_2 + (NH_4)_2[IrCl_6] \rightarrow [Ir_xRu_{1\text{-}x}(NH_3)_5Cl][IrCl_6]$;

thermal decomposition in H_2 flow: $[Ir_xRu_{1\text{-}x}(NH_3)_5Cl][IrCl_6] \rightarrow Ir_{0.5+x/2}Ru_{0.5\text{-}x/2}$.

Following the similar strategy, it was also possible to extend our approach to access Ir–Os–Ru ternary alloys, which were prepared using thermal decomposition of multimetallic coordination compounds as single-source precursors.

Crystallization from water solution: $x[Ir(NH_3)_5Cl]Cl_2 + (1\text{-}x)[RuNH_3)_5Cl]Cl_2 + y(NH_4)_2[OsCl_6] + (1\text{-}y)(NH_4)_2[IrCl_6] \rightarrow [Ir_xRu_{1\text{-}x}(NH_3)_5Cl][Os_yIr_{(1\text{-}y)}Cl_6]$;

thermal decomposition in H_2 flow: $[Ir_xRu_{1\text{-}x}(NH_3)_5Cl][Os_yIr_{(1\text{-}y)}Cl_6] \rightarrow Ir_{0.5+x/2\text{-}y/2}Ru_{0.5\text{-}x/2}Os_{y/2}$.

IR- and Raman spectra of multimetallic coordination compounds (Figure 1) a similar to to their precursors. IR-spectra of multimetallic complexes $[Ir_xRu_{1\text{-}x}(NH_3)_5Cl][Os_yIr_{(1\text{-}y)}Cl_6]$ show slight shifts in comparison with $[Ir(NH_3)_5Cl]Cl_2$, $[RuNH_3)_5Cl]Cl_2$, $(NH_4)_2[OsCl_6]$, and $(NH_4)_2[IrCl_6]$ due to variations in ionic fields related, among others, to particles morphology. With increasing of amount of $[IrCl_6]^{2-}$, $\nu(M\text{–Cl})$ shifts from 314 to 321 cm^{-1}. With increasing of amount of $[Ir(NH_3)_5Cl]^{2+}$, $\nu(M\text{–N})$ shifts from 448 to 470 cm^{-1}. $\nu(M\text{–N})$ is visible in pure double complex salts but nearly disappears in multimetallic $[Ir_xRu_{1\text{-}x}(NH_3)_5Cl][Os_yIr_{(1\text{-}y)}Cl_6]$ due to its broadness. A similar tendency has been obtained for Raman spectra.

Nominal compositions were chosen to follow a *quasi*-binary Ir–$Os_{0.5}Ru_{0.5}$ cross-section of the ternary Ir–Os–Ru phase diagram. Resulting alloys elemental composition corresponds to the composition of starting water solutions without a visible systematic enrichment with one of the metals (Table 1, Figure 2). A variation in composition allowed us to cover the whole ternary

phase diagram and can be considered as a unique approach for the preparation of ternary alloys in the whole concentration interval [12, 27].

3.2. Thermal decomposition of single-source precursors

$[Ir_xRu_{1-x}(NH_3)_5Cl][Os_yIr_{(1-y)}Cl_6]$ multimetallic single-source precursors can be considered as solid solutions of $[Ru(NH_3)_5Cl][IrCl_6]$, $[Ir(NH_3)_5Cl][IrCl_6]$, $[Ru(NH_3)_5Cl][OsCl_6]$, and $[Ir(NH_3)_5Cl][OsCl_6]$ bimetallic double complex salts where cations and anions are substituted in their crystal structures. Recently, thermal decomposition processes of $[Ru(NH_3)_5Cl][IrCl_6]$ and $[Ir(NH_3)_5Cl][IrCl_6]$ as well as mixed $[Ir_xRu_{1-x}(NH_3)_5Cl][IrCl_6]$ salts were already investigated using DSC, *in situ* and *ex situ* IR- and Raman-spectroscopy. It has been shown that Ru-rich compounds show a significantly high exothermal effect which can be related to simultaneous reduction of Ir(IV) from the anionic part and Ru(III) from the cationic side of the double complex salt [30]. Nevertheless, crystalline intermediates as well as metallic particles formed on early stages of thermal decomposition were not detected due to absence of high temperature *in situ* or *ex situ* PXRD data.

Detailed knowledge about thermal decomposition of $[Ir(NH_3)_5Cl][OsCl_6]$ sheds light on the understanding of nanostructured alloys formation process upon heating of chemically and structurally similar salts $[(Ir/Rh/Ru/Co/Os)^{III}(NH_3)_5Cl][(Re/Ir/Pt/Os)^{IV}Cl_6]$. It has been shown that salts containing Ir(IV) in their anionic parts, namely $[(Ru/Co/Cr/Rh)^{III}(NH_3)_5Cl][IrCl_6]$ have pronounced exothermic effect upon their thermal decomposition [30]. In contrast, $[Ir(NH_3)_5Cl][OsCl_6]$ based on Os(IV) anion does not show any exothermic processes upon its thermal decomposition.

In reductive atmosphere (5 vol.% H_2 in He), $[Ir(NH_3)_5Cl][OsCl_6]$ decomposes at lower temperatures above 450 K with a formation of mixture that contains $(NH_4)_2[OsCl_6]$ and metallic phase with broad reflexes which might be a defect *fcc*-structured phase (Figures 3A and 3B). Further heating results in decomposition of $(NH_4)_2[OsCl_6]$ with a formation of *fcc*+*hcp* two-phase mixture; further heating above 500 K gives a pure *hcp*–$Ir_{0.5}Os_{0.5}$ alloy as a single phase.

Single-phase *hcp*–$Ir_{0.5}Os_{0.5}$ corresponds to the miscibility gap of Ir–Os phase diagram and should be metastable.

In inert atmosphere, $[Ir(NH_3)_5Cl][OsCl_6]$ decomposes above 850 K and forms a two-phase *fcc+hcp* mixture without formation of any crystalline intermediates (Figures 3B and 3C). Upon further heating, a phase exchange results in a formation of *fcc*-structured alloy as a major phase with a minor admixture of *hcp*-structured alloy. Such phase separation has been described previously for other Ir–Os alloys prepared from $(NH_4)_2[Ir_xOs_{1-x}Cl_6]$ [7, 8].

In situ investigation of $[Ir(NH_3)_5Cl][OsCl_6]$ suggests the decomposition pathways for other precursors from $[(Ir/Rh/Ru/Co/Os)^{III}(NH_3)_5Cl][(Re/Ir/Pt/Os)^{IV}Cl_6]$ family. In reductive atmosphere, compounds might form $(NH_4)_2[(Re/Ir/Pt/Os)^{IV}Cl_6]$ as crystalline intermediates; metals from their cationic parts are reduced by hydrogen with formation of defect metallic particles. Final metallic products of thermal decomposition in reductive atmosphere might be single-phase and metastable under ambient conditions. In inert atmosphere, salts decompose at higher temperature without formation of any crystalline intermediates. Metallic particles obtained in inert atmosphere are usually two-phase mixtures and correspond to thermodynamically stable compositions suggested by equilibrium phase diagrams.

Final products consist of relatively large aggregates of particles. Particle's shape follows regular shape of single-source precursor's crystal form (Figure 4). Similar behaviour is typical for products of thermal decomposition of double complex salts (see examples given in [31–32]) and not surprising in the current system.

3.3. Ir–Os–Ru ternary phase diagram

Ru and Os are completely miscible in solid and liquid states [33]. Based on published experimental data, binary Os–Ru alloys can be considered as ideal in both, solid and liquid states [33]. Ir–Ru and Ir–Os peritectic phase diagrams were experimentally investigated in detail by several independent research groups [34–38] and can be considered as well-known complete and

correct binary diagrams at least in their solidus parts. Nevertheless, both diagrams were not investigated in many details in the liquid state and require a further improvement at higher temperatures. To assess both diagrams, a sub-regular solutions model should be applied. Access Gibbs energy for non-ideal solutions should be written as the following:

$$G^{xs} = x_A x_B \sum_{i=0}^{n} L_{AB} ¿¿¿ \qquad \text{(Equation 1).}$$

Both Ir–Ru and Ir–Os peritectic systems cannot be described using the ideal solutions model. Only a sub-sub-regular model gives satisfactory results. The best fits between experimental and calculated phase diagrams were obtained with the following mixing parameters:

$$^{\circ}L^{liq}_{Ir,Os} = ¿\ 16644 + 3.5 \cdot T + 0.4 \cdot T \cdot lnT;$$

$$^{\circ}L^{hcp}_{Ir,Os} = ¿ -23064 - 19.9 \cdot T + 4.9 \cdot T \cdot lnT;$$

$$^{\circ}L^{fcc}_{Ir,Os} = ¿\ -37608 - 19.2 \cdot T + 5.1 \cdot T \cdot lnT;$$

$$^{\circ}L^{liq}_{Ir,Ru} = ¿ 32348 - 10.4 \cdot T;$$

$$^{\circ}L^{hcp}_{Ir,Ru} = ¿ 9895 - 3.9 \cdot T;$$

$$^{\circ}L^{fcc}_{Ir,Ru} = ¿\ -3621 - 1.5 \cdot T.$$

Aforementioned mixing parameters can be used to access ternary Ir–Os–Ru phase diagram. Experimental Ir–Os–Ru ternary phase diagram has not been yet described in the literature. Nevertheless, it can be modelled using CALPHAD approach based on the binary thermodynamic database for Ir–Os, Ir–Ru and Os–Ru binary diagrams described above. Figure 2 shows isothermal and isoconcentrate cross-sections of Ir–Os–Ru ternary diagram obtained using the ideal solutions model and mixing parameters for three binary systems. Single- and two-phase Ir–Os–Ru samples prepared from single-source precursors satisfactorily match the sub-regular modelled phase diagram. Nevertheless, appearance of two-phase $Ir_{0.68}Ru_{0.13}Os_{0.19}$ composition in the *fcc* stability region suggests a significance of ternary mixing parameter for the final model of the phase diagram. Our analysis suggests that thermal decomposition of multimetallic single-source precursors gives mainly thermodynamically stable ternary alloys which likely fits stability regions of ternary phase diagram. Samples which correspond to miscibility gap of the ternary phase diagram, are likely be two-phase. Similarly, a model for Ir–Os–Ru ternary phase diagram

obtained by Cabri and Harris [6] based on natural iridosmine samples also corresponds well with the modelled phase diagram obtained using mixing parameters characteristic for Ir–Os, Ir–Ru and Os–Ru binary systems.

3.4. Thermal expansion and pressure compressibility of Ir–Ru binary and Ir–Os–Ru ternary alloys

Single-phase *fcc*- and *hcp*-structured Ir–Os [7, 8], Ir–Ru [11], and Ir–Os–Ru alloys can be considered as synthetic analogous to obtain thermal expansion and pressure compressibility curves for iridosmine minerals (Figures 5 and 6). Thermal expansion parameters for pure Ir, Os and Ru are very similar, nevertheless, both single-phase ternary alloys show a lower thermal expansion compared to with pure metals. Similar effect has been noted for Ir–Re and Ir–Os binaries where thermal expansion was also obtained to be lower in comparison with pure Ir, Re and Os. *Hcp*-structured alloy shows a growth of *c/a* value with temperature similar to *c/a* behaviour of pure *hcp*-structured Os and Ru [39,43].

All investigated alloys show a regular room temperature compression below 40–45 GPa. *c/a* value for *hcp*-structured alloy increases with pressure, similarly to other *hcp*-structured refractory alloys in Ir–Re and Ir–Os binary systems. Surprisingly, *fcc*–$Ir_{0.84}Ru_{0.06}Os_{0.10}$ as well as *fcc*–$Ir_{0.75}Ru_{0.25}$ and *hcp*–$Ir_{0.33}Ru_{0.67}$ alloys show significantly smaller bulk modulus within comparison with pure metals. Such behaviour is quite unusual and might be a sign of substantial chemical and electronic interactions between naturally (?) *fcc*-structured Ir and *hcp*-structured Ru [40]. A strongly different long-range magnetic ordering found in *fcc*–$Ir_{0.75}Ru_{0.25}$ and *hcp*–$Ir_{0.33}Ru_{0.67}$ alloys at low temperature as well as a presence of several magnetic phase transitions revealed by the temperature dependent magnetic susceptibility (see magnetic data below) supports an assumption about a strong influence of electronic configurations and hybridization effects on properties of entire systems. Ir–Os binary alloys do not show such an effect upon compression giving a sign that the observed compressibility irregularity corresponds specifically to Ir interaction with Ru.

Compressibility of binary *fcc*–$Ir_{0.75}Ru_{0.25}$ and *hcp*–$Ir_{0.33}Ru_{0.67}$ alloys is higher in comparison with pure metals. At all pressures, V/V_0 values for *hcp*–$Ir_{0.33}Ru_{0.67}$ alloy follow visibly below corresponding values for Ir and Ru (Figure 6). For *fcc*–$Ir_{0.75}Ru_{0.25}$, a relative compressibility is similar to pure Ir and Ru (Figure 6). Such behaviour might correspond to a difference in atomic volumes of Ir and Ru (14.1475 and 13.575 $Å^3 \cdot atom^{-1}$, respectively) with very close equal bulk moduli (341 and 348 GPa, respectively).

Bulk moduli for binary alloys can be estimated using the ideal solutions model reported in [43]. Concentration dependence of the bulk modulus $B_0(x)$ of binary metallic alloy $M^1_x M^2_{1-x}$ containing x atomic fraction of refractory metal can be calculated using the following equation:

$$B_0(x) = B_2 \left[\frac{1 + x\left(\frac{V_1}{V_2} - 1\right)}{1 + x\left(\frac{B_2 V_1}{B_1 V_2} - 1\right)} \right] \qquad \text{(Equation 2)},$$

where B_1 and B_2 (GPa) are the bulk moduli of M^1 and M^2 metals, and V_1 and V_2 ($Å^3$) are atomic volumes of these metals at ambient pressure, correspondingly.

Estimations based on Equation 2 as well as experimental data for six Ir–Ru and Ir–Os binary alloys are summarized in Table 2. Bulk moduli for Ir–Ru binary alloys are significantly smaller compared to pure Ir and Ru. Ir and Ru have nearly identical bulk moduli but the difference in their atomic volumes is relatively large and seems to be more important for compressibility of their binary alloys. According to Equation 2, the bulk modulus for an alloy depends on both parameters, bulk moduli and atomic volumes, of individual metals; nevertheless, identical bulk moduli of components result in independence of alloys compressibility on composition, which is equivalent to Zen's rule [46, 47] for dependence of atomic volumes of alloys on their compositions. Alternative approach has been used by Sarlis and Skordas [48]: Their model includes not only a variation in composition but also a variation in atomic volumes of each binary alloy in the series. Nevertheless, this alternative approach cannot predict the smaller bulk moduli for Ir–Ru binary alloys and the larger bulk moduli for Ir–

Os system without considering incorrectness in the experimental bulk moduli of pure Os and Ru. Alloys containing only *fcc*- or only *hcp*-structured metals such as *fcc*–$Ir_{0.42}Rh_{0.58}$ show a regular composition dependence of their compressibility and can be estimated according to Equation 2 (experimental and theoretical values were found to be 317(17) and 316.9 GPa, correspondingly [42]). Our findings suggest that theory of alloys between *fcc*- and *hcp*-structured metals have to be intensively developed to be able to predict their correct compressibility parameters. In binary systems such as Ir–Ru and Ir–Os, Equation 2 seems to be less precise and does not give reliable values. Nevertheless, precise data for compositional dependence of bulk moduli for ternary and multicomponent alloys might be used to predict a compressibility of multicomponent refractory alloys.

Similar to binary *fcc*–$Ir_{0.75}Ru_{0.25}$ system, relative compressibility of ternary *fcc*–$Ir_{0.84}Ru_{0.06}Os_{0.10}$ alloy is significantly lower compared to pure metals. Its V/V_0 pressure dependence curve is lower in comparison with pure metals which is also a sign for existence of some peculiarities in its crystal and electronic structure and might be associated with relatively large differences in atomic volumes of Os and Ir from one hand and Ru from the other hand. An influence of effective "*free*" volume between various atoms in the crystal structure should be also considered. In general, bulk moduli of transition metals can be correlated with a number of *d*-electrons [49]. For alloys of elements from various transition metal series, electron correlations may play a critical role resulting in a complex compositional dependence of bulk moduli. Our experimental findings should be considered as a starting point of deep theoretical modelling to explain such a phenomenon.

As it has been shown for Ir–Re, Ir–Os and Os–Pt binary phase diagrams [48–50], phase diagrams constitution and concentration windows for miscibility gaps between *fcc*- and *hcp*-structured alloys depend on pressure not only for systems with a high compressibility but also for systems with an extremely low compressibility, such as Ir–Os. Irregularities in bulk moduli of Ir–Ru alloys and especially in ternary Ir–Ru–Os alloys with a relatively high compressibility of

fcc-structured ternary alloy give a sign that Ir–Ru–Os phase diagram might have large pressure changes. Pressure transformation of ternary Ir–Ru–Os phase diagram should play an important role in formation of iridosmine minerals and should be taken into account.

3.5. Magnetic susceptibility of Ir–Ru binary alloys

Magnetic properties of Ir–Ru binary alloys might indicate a strong impact of interatomic interactions on their behaviour under variable temperatures and compression. *fcc*–$Ir_{0.75}Ru_{0.25}$ and *hcp*–$Ir_{0.33}Ru_{0.67}$ alloys reveal a very different magnetic behaviour at low temperature of 10 K (Figure 7): field dependence for *hcp*–$Ir_{0.33}Ru_{0.67}$ shows a dominant diamagnetic response while *fcc*–$Ir_{0.75}Ru_{0.25}$ exhibits an expected (due to electronic configurations of constituents) paramagnetic-like behaviour. No reasonable signal was detected for *hcp*–$Ir_{0.33}Ru_{0.67}$ alloy at room temperature contrary to *fcc*–$Ir_{0.75}Ru_{0.25}$ one. The temperature dependence of magnetisation recorded for *fcc*–$Ir_{0.75}Ru_{0.25}$ alloy in the temperature range of 2–360 K in 500 Oe magnetic field shows a rather complex tendency. It could be assumed that there are several magnetic phase transitions (at approx. 3.4 K, 135 K and 233 K) related to magnetic phases with different Curie and/or Neel temperatures as well as to the reorientation of Ru and Ir magnetic moments inside of the crystallographic matrix. Some structural transitions below room temperature also could not be fully excluded.

In general, magnetic properties of Ir-based alloys, complexes, and oxides demonstrate a non-trivial magnetic behaviour. Thus, *fcc*–Fe_xIr_{1-x} alloys exhibit very different temperature dependence of magnetic susceptibility depending on iron concentration [53 and references therein]. For $x < 0.05$ the magnetic susceptibility does not follow the Curie-Weiss law but decreases with increasing temperature; for $0.05 < x < 0.35$, an antiferromagnetic-like maximum is present and the temperature of this maximum increases with increasing iron concentration; for x above 0.35 the susceptibility increases with temperature rising. The Mössbauer spectra measurements performed on *fcc*–$Fe_{0.30}Ir_{0.70}$ clarified the origin of such a susceptibility peak observed at 40 K and confirmed the presence of an antiferromagnetic spin-ordering below this

temperature. In Pt-substituted *fcc*–$Fe_{65}(Pt_yIr_{1-y})_{35}$ disordered alloy, the ferromagnetic ordering observed over a composition range for $y > 0.7$ shows the magnetization and the Curie temperature increase with increasing y, but it switches to an antiferromagnetic one for y below 0.7 [54].

Density functional theory modelling of magnetic Ir_n clusters (n = 2–15) within the generalized gradient approximation suggests a dominating 5d character of magnetic properties with sizable values of magnetic moments in the range of 1–2 μBohr per Ir atom for small Ir_n clusters with $n < 8$ and a sharp decrease of magnetic moments down to 0–0.5 μBohr per Ir atom in larger Ir_n clusters with $8 < n < 15$ [55]. Clustering of Ir in investigated alloys might also play an important role in their magnetic behaviour.

Mössbauer spectroscopy studies performed on Ru_xFe_{1-x} alloys demonstrate a presence of antiferromagnetic ordering with Neel temperatures dependent on Ru concentration (210 K and 60 K for $x = 0.15$ and $x = 0.3$, respectively), while Ru_yOs_{1-y} alloy shows a lower Neel temperature of 30 K for $x = 0.15$ and no sign of magnetism at any temperature for $x = 0.3$ [56].

Being isoelectronic with iron, Ru is often used as Fe substitute for modifying the properties of superconducting iron-based compounds [57–59] where it does not change the value of the chemical potential and acts similar as magnetic dilution [59]; as an impurity in iron host Ru could carry a noticeable magnetic moment of 0.9 ± 0.5 μBohr per atom [60, 61]. In a series of single-crystalline $R_2Fe_{17-x}Ru_x$ (R = Y, Lu, Er) alloys a ferro- or ferrimagnetic ordering of a parent alloy was found to be destroyed by Ru doping and a complicated nature of antiferromagnetic ordering was revealed [62]. In $Lu_2Fe_{16.5}Ru_{0.5}$ a small magnetic moment of Ru was found to be aligned parallel to the dominant Fe sublattice magnetization [63].

Despite bulk *hcp*-Ru as well as *hcp*-Os is paramagnetic, theoretical calculations have proposed that Ru and Os could be ferromagnetic if they are forced into a tetragonal lattice structure [64] which for Ru could be realized experimentally only in ultrathin films where it may also have a large perpendicular MCA due to Jahn–Teller splitting [65].

Therefore, more precise studies of magnetic phases found in *fcc*-$Ir_{0.75}Ru_{0.25}$ require element-specific investigations with polarized hard X-rays from synchrotron sources. To unravel peculiarities of Ir and Ru electronic configurations, the magnetic ordering of species on the local scale and their impact on properties of the entire system, X-ray absorption spectroscopy (XAS) in combination with X-ray magnetic circular dichroism (XMCD) technique at the Ru-$L_{2,3}$ and Ir-$L_{2,3}$ absorption edges have to be applied. It will highlight the differences in electronic and magnetic interactions between the currently studied Ir-based alloys and Ir-based perovskites previously explored by X-ray resonant magnetic scattering (XRMS) [66], XAS/XMCD [67] and Nuclear resonance scattering (NRS) [68] besides the differences from pure Os, Ir and Ru taken by NRS [68–70] and Ru in $Lu_2Fe_{16.5}Ru_{0.5}$ by XAS/XMCD [63].

Conclusions

Binary and ternary *fcc*- and *hcp*-structured alloys based on Ir, Ru and Os can be prepared from single-source precursors under relatively low temperature. $[Ir_xRu_{1-x}(NH_3)_5Cl][Os_yIr_{(1-y)}Cl_6]$ multimetallic single-source precursors can be successfully used to obtain ternary *hcp*–$Ir_{0.24}Ru_{0.36}Os_{0.40}$ and *fcc*–$Ir_{0.84}Ru_{0.06}Os_{0.10}$ alloys. Their phase composition matches the ternary phase diagram which was modelled based on thermodynamic database for binary Ir–Ru, Ir–Os and Ru–Os systems. Thermal decomposition of a parent compound, $[Ir(NH_3)_5Cl][OsCl_6]$ has been investigated in inert and reductive atmospheres. Decomposition mechanism was found to be dependent on atmosphere. In inert atmosphere, no crystalline intermediates were found. The final product of heating above 870 K is a mixture of *fcc*- and *hcp*-structured alloys which is in accordance with the existing Ir–Os phase diagram. In reductive atmosphere, $(NH_4)_2[OsCl_6]$ has been detected as an intermediate phase. Further heating results in formation of metastable single-phase *hcp*–$Ir_{0.5}Os_{0.5}$ alloy.

Room temperature compressibility of *hcp*–$Ir_{0.24}Ru_{0.36}Os_{0.40}$ and *fcc*–$Ir_{0.84}Ru_{0.06}Os_{0.10}$ ternary alloys as well as *hcp*–$Ir_{0.33}Ru_{0.67}$ and *fcc*–$Ir_{0.75}Ru_{0.25}$ binary alloys has been characterized using powder PXRD in diamond anvil cells. Below 46 GPa, all alloys show regular compressibility

without phase transformations. *Hcp*–$Ir_{0.33}Ru_{0.67}$ and *fcc*–$Ir_{0.75}Ru_{0.25}$ binary alloys exhibit higher compressibility in comparison with pure metals. Ternary alloys show lower thermal expansion in comparison with pure metals. High bulk moduli characteristic for investigated alloys can be correlated with their complex magnetic behaviour. *Fcc*–$Ir_{0.75}Ru_{0.25}$ alloy reveals several magnetic phases below room temperature.

Acknowledgements

The authors thank the I11 beamline at the DIAMOND LS, UK; the ID11, BM01A, and ID15B beamlines at the European Synchrotron Radiation Facility, Grenoble, France, for providing us with measurement time and technical support. Study has been partially carried on the P02.1 beamline at the PETRA III synchrotron facility at DESY (Hamburg), a member of the Helmholtz Association (HGF). A.S. acknowledges personal funding from CALIPSOplus project (the Grant Agreement 730872 from the EU Framework Programme for Research and Innovation HORIZON 2020).

References:

1. G. Raykhtsaum, PGM Highlights: Platinum Alloys: A Selective Review of the Available Literature, Platinum Metals Rev., 57(3) (2013), 202–213. DOI: 10.1595/147106713x668596

2. L.J. Cabri, The platinum group minerals / In: The Geology, Geochemistry, Mineralogy and mineral Beneficiation of platinum group elements. Spec. Vol. 54. Canadian Inst. of Mining, Metalurgy, and Petroleum, 2002, P. 13–131.

3. J.M. Bird, W.A. Bassett, Evidence of a Deep Mantle History in Terrestrial Osmium-Iridium-Ruthenium Alloys, J. Geophys. Res., 85 (1980), 5461–5470. DOI: 10.1029/JB085iB10p05461

4. R.O.C. Fonseca, V. Laurenz, G. Mallmann, A. Luguet, N. Hoehne, K.P. Jochum, New constraints on the genesis and long-term stability of Os-rich alloys in the Earth's mantle, Geochim. Cosmochim. Acta, 87 (2012), 227–242. DOI: 10.1016/j.gca.2012.04.002

5. D.C. Harris, L.J. Cabri, Nomenclature of platinum-group-element alloys: review and revision, Can. Miner., 29 (1991), 231–237.

6. L.J. Cabri, D.C. Harris, T.W. Weiser, Mineralogy and Distribution of Platinum-group Mineral (PGM) Placer Deposits of the World, Exploration and Mining Geology, 5(2) (1996), 73–167.

7. K.V. Yusenko, E. Bykova, M. Bykov, S.A. Gromilov, A.V. Kurnosov, C. Prescher, V.B. Prakapenka, M. Hanfland, S. van Smaalen, S. Margadonna, L.S. Dubrovinsky, Compressibility of Ir–Os alloys under high pressure, J. Alloys Comp., 622 (2015), 155–161. DOI: https://doi.org/10.1016/j.jallcom.2014.09.210

8. K.V. Yusenko, E. Bykova, M. Bykov, S.A. Gromilov, A.V. Kurnosov, C. Prescher, V. Prakapenka, W.A. Crichton, M. Hanfland, S. Margadonna, L.S. Dubrovinsky, High-pressure high-temperature stability of *hcp*–Ir_xOs_{1-x} (x = 0.50 and 0.55) alloys, J. Alloys Comp., 700 (2017), 198–207. DOI: https://doi.org/10.1016/j.jallcom.2016.12.207

9. Yu.V. Shubin, S.V. Korenev, K.V. Yusenko, T.M. Korda, A.B. Venediktov, Powder X-ray diffraction study of the double complexes $[M(NH_3)_5Cl][M'Cl_4]$ as precursors of metal powders (M = Ir, Rh, Co; M' = Pt, Pd), Russ. Chem. Bull. 51(1) (2002), 41–45. DOI: 10.1023/A:1015045310216

10. S.A. Martynova, K.V. Yusenko, I.V. Korolkov, S.A. Gromilov, Synthesis, properties, and thermal decomposition products of $[Ru(NH_3)_5Cl][PtCl_6]$ and $[Ru(NH_3)_5Cl]_2[PtCl_6]Cl_2$, Russ. J. Coord. Chem., 33(7) (2007), 530–534. DOI: 10.1134/S1070328407070093

11. S.A. Martynova, K.V. Yusenko, I.V. Korolkov, S.A. Gromilov, Solid solutions Ru_xIr_{1-x} synthesized by thermolysis of coordination compounds, Russ. J. Inorg. Chem., 52(11) (2007), 1733–1738. DOI: 10.1134/S0036023607110162

12. K.V. Yusenko, S. Riva, P.A. Carvalho, M.V. Yusenko, S. Arnaboldi, A. Sukhikh, M. Hanfland, S.A. Gromilov, First hexagonal close packed high-entropy alloy with outstanding stability under extreme conditions and high electrocatalytic activity in methanol oxidation, Scripta Materialia, 138 (2017), 22–27. DOI: 10.1016/j.scriptamat.2017.05.022

13. S.P. Thompson, J.E. Parker, J. Marchal, J. Potter, A. Birt, F. Yuang, R.D. Fearn, A.R. Lennie, S.R. Street, C.C. Tang, Fast X-ray powder diffraction on I11 at Diamond. J. Synchrotron Rad. 18 (2011), 637–748. DOI: 10.1107/S0909049511013641.

14. V. Dyadkin, SNBL Tool-box. Grenoble, France: Swiss Norwegian Beamline at ESRF, 2013.

15. P. Rajiv, R. Dinnebier, M. Jansen, Powder 3D Parametric: A program for automated sequential and parametric Rietveld refinement using Topas, Materials Science Forum, 651 (2010), 97–104. DOI: https://doi.org/10.4028/www.scientific.net/MSF.651.97

16. PDF–2 Release 2012 (Database), ed. S. Kabekkodu, International Centre for Diffraction Data, Newtown Square, PA, USA (2012)

17. I. Kantor, V. Prakapenka, A. Kantor, P. Dera, A. Kurnosov, S. Sinegeikin, N: Dubrovinskaia, L. Dubrovinsky, BX90: A new diamond anvil cell design for X-ray diffraction and optical measurements. Rev. Scientific Inst. 83 (2012), 125102. DOI: https://doi.org/10.1063/1.4768541

18. A. Kunrosov, I. Kantor, T. Boffa-Ballaran, S. Lindhradt, L. Dubrovinsky, A. Kuznetsov, B.H. Zehlender, A novel gas-loading system for mechanically closing of various types of diamond anvil cells. Rev. Scientific Inst. 79 (2008), 045110. DOI: https://doi.org/10.1063/1.2902506

19. Yingwei Fei, A. Ricolleau, M. Frank, K. Mibe, Guoyin Shen, V. Prakapenka, Toward an internally consistent pressure scale. PNAS 104(22) (2007), 9182–9186. DOI: https://doi.org/10.1073/pnas.0609013104

20. C. Prescher, V.B. Prakapenka, DIOPTAS: a program for reduction of two-dimensional X-ray diffraction data and data exploration, High Press. Res. 35(3) (2015), 223–230. DOI: https://doi.org/10.1080/08957959.2015.1059835

21. V. Petříček, M. Dušek, L. Palatinus, Crystallographic computing system JANA2006: General Features. Z. Krist 229(5) (2014), 345–352. DOI: 10.1515/zkri-2014-1737; http://www-xray.fzu.cz/jana/jana.html

22. R.J. Angel, Equations of State. In Hazen, R.M., Downs, R.T. (Eds.), High-pressure, high-temperature crystal chemistry, Reviews in Mineralogy and Geochemistry, 41 (2001), 35–60. DOI: https://doi.org/10.2138/rmg.2000.41.2; http://www.rossangel.com

23. S.-L. Chen, S. Daniel, F. Zhang, Y.A. Chang, X.-Y. Xie, R. Schmid-Fetzer, W.A. Oates, The PANDAT Software Package and its Applications, CALPHAD, 26(2) (2002), 175–188. DOI: https://doi.org/10.1016/S0364-5916(02)00034-2

24. A.T. Dinsdale, SGTE data for elements, CALPHAD, 15(4) (1991), 317–425; http://www.sgte.org/; DOI: https://doi.org/10.1016/0364-5916(91)90030-N

25. S.V. Korenev, A.B. Venediktov, Yu.V. Shubin, S.A. Gromilov, K.V. Yusenko, Synthesis and structure of binary complexes of platinum group metals – precursors of metallic materials, J. Struct. Chem., 44(1) (2003), 46–59. DOI: 10.1023/A:1024980930337

26. S.I. Pechenyuk, D.P. Domonov, Properties of Binary Complex Compounds, J. Struct. Chem., 52(2) (2011), 412–427. DOI: https://doi.org/10.1134/S0022476611020259

27. S.V. Korenev, S.A. Gromilov, A.I. Gubanov, A.B. Venediktov, $[Pd(NH_3)_4][Ir_{0.5}Os_{0.5}Cl_6]$ solid solution: Synthesis and properties, Russ. J. Coord. Chem., 29(3) (2003), 219–221. DOI: 10.1023/A:1022840016102

28. I.V. Korolkov, S.A. Gromilov, K.V. Yusenko, I.A. Baidina, S.V. Korenev, Crystal structure of the $[Ir(NH_3)_5Cl]_2[OsCl_6]Cl_2$. Crystal analysis of the Ir–Os metallic system, J. Structural Chemistry, 46(6) (2005), 1052–1059. DOI: 10.1007/s10947-006-0241-8

29. I.V. Korolkov, S.A. Martynova, K.V. Yusenko, S.V. Korenev, Double complex salts with $[Ru(NH_3)_5Cl]^{2+}$ cation and $[OsCl_6]^{2-}$ anion: Synthesis and properties. Crystal structure of $[Ru(NH_3)_5Cl]_2[OsCl_6]Cl_2$, Russ. J. Inorg. Chem., 55(9) (2010), 1347–1351. DOI: 10.1134/S0036023610090032

30. S.A. Martynova, P.E. Plusnin, T.I. Asanova, I.P. Asanov, D.P. Pischur, S.V. Korenev, S.V. Kosheev, S. Floquet, E. Cadot, K.V. Yusenko, Exothermal effect in the thermal decomposition

of $[IrCl_6]^{2-}$-containing salts with $[M(NH_3)_5Cl]^{2+}$ cations: $[M(NH_3)_5Cl][IrCl_6]$ (M = Co, Ru, Cr, Rh , Ir) New Journal of Chemistry, 42(3) (2018), 1762–1770. DOI: 10.1039/c7nj04035k

31. M. Avisar-Levy, O. Levy, O. Ascarelli, I. Popov, A. Bino, Fractal structures of highly-porous metals and alloys at the nanoscale, J. Alloys Comp. 635(25) (2015) 48–54 http://dx.doi.org/10.1016/j.jallcom.2015.02.073

32. S.A. Gromilov, Yu.V. Shubin, A.I. Gubanov, E.A. Maksimovskii, S.V. Korenev, X-ray study of the thermolysis products of $(NH_4)_2[OsCl_6]_x[PtCl_6]_{1-x}$. J. Struct. Chem., 50 (2009), 1121– 1125. https://doi.org/10.1007/s10947-009-0164-2

33. K.V. Yusenko, I.V. Korolkov, S.A. Martynova, S.A. Gromilov, Ru–Re, Ru–Os and Re–Os solid solutions — preparation under mild conditions, powder XRD investigation and phase diagrams analysis, Z. Krist., Suppl. 30 (2009), 269–275. DOI: 10.1524/zksu.2009.0039

34. R.D. Reiswig, J.M. Dickinson, The Osmium-Iridium Equilibrium Diagram, Trans. Metall. Soc. AIME, 230 (1964), 469–472.

35. H. Okamoto, The Ir–Os (Iridium–Osmium) System, J. Phase Equilib., 15 (1994), 55–57. DOI: 10.1007/BF02667683

36. H.C. Vacher, C.J. Bechtoldt, E. Maxwell, Structure of Some Iridium–Osmium Alloys, J. Metals, 200(1) (1954), 80–82.

37. T. H. Gebali, E B. T. Matthias V. B. Compton, E. Corenzwit, D G. W. Hull JR., Superconductivity of Solid Solutions of Noble Metals, Phys. Rev. 129(1) (1963), 182–183. DOI: http://dx.doi.org/10.1103/PhysRev.129.182

38. R.S. Rudman, Lattice parameters of some h.c.p. binary alloys of rhenium and osmium: Re–W, Re–Ir, Re–Pt; Os–Ir, Os–Pt, J. Less-Common Metals, 12(1) (1967), 79–81. DOI: 10.1016/0022-5088(67)90075-6

39. J.W. Arblaster, Crystallographic Properties of Osmium, Platinum Met. Rev., 57 (2013), 177–185. DOI: 10.1595/147106713x668541

40. L. Dubrovinsky, N. Dubrovinskaia, E. Bykova, M. Bykov, V. Prakapenka, C. Prescher, K. Glazyrin, H.-P. Liermann, M. Hanfland, M. Ekholm, Q. Feng, L. V. Pourovskii, M. I. Katsnelson, J. M. Wills, I.A. Abrikosov, The most incompressible metal osmium at static pressures above 750 gigapascals, Nature, 525 (2015), 226–229. DOI: https://doi.org/10.1038/nature14681

41. J.W. Arblaster, Crystallographic Properties of Iridium, Platinum Met. Rev., 54 (2010), 93–102. DOI: 10.1595/147106710x493124

42. K.V. Yusenko, S. Khandarkhaeva, T. Fedotenko, A. Pakhomova, S.A. Gromilov, L. Dubrovinsky, N. Dubrovinskaia, Equations of state of Rhodium, Iridium and their alloys up to 70 GPa, J. Alloys Comp., 788 (2019), 212–218. DOI: https://doi.org/10.1016/j.jallcom.2019.02.206

43. J.W. Arblaster, Crystallographic Properties of Ruthenium, Platinum Met. Rev., 57 (2013), 127–136. DOI: 10.1595/147106713x665030

44. Hyunchae Cynn, J.E. Klepeis, Choong-Shik Yoo, D.A. Young, Osmium has the Lowest Experimentally Determined Compressibility, Phys Rev Lett, 88(13) (2002), 135701-1. DOI: https://doi.org/10.1103/PhysRevLett.88.135701

45. P. Varotsos, K. Alexopoulos, In Thermodynamics of point defects and their relation with bulk properties. Series, Defects in solids, Amelinckx, S., Gevers, R., Nihoul, J., Eds.; North-Holland Publ. Co.: Amsterdam, 1986; P. 156–158 and P. 325–347.

46. Zen E-an, Validity of “Vegard’s Law”, American Mineralogist, 41 (1956), 523–524.

47. A.R. Denton, N.W. Ashcroft, Vegard's Law, Physical Review A, 43 (1991), 3161. DOI: https://doi.org/10.1103/PhysRevA.43.3161

48. N.V. Sarlis, E.S. Skordas, Estimating the Compressibility of Osmium from Recent Measurements of Ir–Os Alloys under High Pressure, J. Phys. Chem. A, 120 (2016), 1601−1604. DOI: https://doi.org/10.1021/acs.jpca.6b00846

49. D. Pettifor, Structure and bonding of molecules and solids, Oxf. Un. Press. (1995), P. 188–189.

50. K.V. Yusenko, K. Spektor, S. Khandarkhaeva, T. Fedotenko, A. Pakhomova, I. Kupenko, A. Rohrbach, S. Klemme, W.A. Crichton, T.V. Dyachkova, A.P. Tyutyunnik, Y.G. Zainulin, L.S. Dubrovinsky, S.A. Gromilov, Decomposition of single-source precursors under high-temperature high-pressure to access osmium–platinum refractory alloys, J. Alloys Comp., 813 (2020), 152121. DOI: https://doi.org/10.1016/j.jallcom.2019.152121

51. K.V. Yusenko, E. Bykova, S. Riva, M. Bykov, W.A. Crichton, M.V. Yusenko, A. Sukhikh, S. Arnaboldi, M. Hanfland, L.S. Dubrovinsky, S.A. Gromilov, Ir–Re binary alloys under extreme conditions and their electrocatalytic activity in methanol oxidation, Acta Mater., 139 (2017), 236–243. DOI: https://doi.org/10.1016/j.actamat.2017.08.012

52. K.V. Yusenko, E. Bykova, M. Bykov, S.A. Gromilov, A.V. Kurnosov, C. Prescher, V. Prakapenka, W.A. Crichton, M. Hanfland, S. Margadonna, L.S. Dubrovinsky, HP–HT stability of *hcp*–Ir_xOs_{1-x} (x = 0.50 and 0.55) alloys, J. Alloys Comp., 700 (2017), 198–207. DOI: https://doi.org/10.1016/j.jallcom.2016.12.207

53. M. Shiga, The Mössbauer Evidence of Antiferromagnetic Spin-Ordering in Face-Centered Cubic Fe-Ir Alloys, Physica Status Solidi (b), 43(1) (1971), K37-K39. DOI: https://doi.org/10.1002/pssb.2220430156

54. M. Shiga, M. Kosaka, Y. Nakamura, Magnetic properties of face-centered cubic $Fe_{65}(Pt_xIr_{1-x})_{35}$ alloys, Physica Status Solidi (b), 50(1) (1972), 351-358. DOI: https://doi.org/10.1002/pssb.2220500141

55. J. Du, X. Sun, J. Chen, G. Jiang, A Theoretical Study on Small Iridium Clusters: Structural Evolution, Electronic and Magnetic Properties, and Reactivity Predictors, J. Phys. Chem. A, 114(49) (2010), 12825–12833. DOI: https://doi.org/10.1021/jp107366z

56. D. I. C. Pearson, J. M. Williams, ^{57}Fe Mossbauer study of hexagonal phase iron alloys, J. Phys. F: Met. Phys., 9 (1979), 1797. DOI: 10.1088/0305-4608/9/9/010

57. K. Nakamura, R. Arita, H. Ikeda, First-principles calculation of transition-metal impurities in LaFeAsO, Phys. Rev. B, 83 (2011), 144512. DOI: https://doi.org/10.1103/PhysRevB.83.144512

58. M. Tropeano, M. R. Cimberle, C. Ferdeghini, G. Lamura, A. Martinelli, A. Palenzona, I. Pallecchi, A. Sala, I. Sheikin, F. Bernardini, M. Monni, S. Massidda, M. Putti, Isoelectronic Ru substitution at the iron site in $SmFe_{1-x}Ru_xAsO_{0.85}F_{0.15}$ and its effects on structural, superconducting, and normal-state properties, Phys. Rev. B, 81 (2010), 184504. DOI: https://doi.org/10.1103/PhysRevB.81.184504

59. R.S. Dhaka, Chang Liu, R.M. Fernandes, Rui Jiang, C.P. Strehlow, T. Kondo, A. Thaler, J. Schmalian, S.L. Bud'ko, P.C. Canfield, A. Kaminski, What Controls the Phase Diagram and Superconductivity in Ru-Substituted BaFe2As2? Phys. Rev. Lett., 107 (2011), 267002. DOI: https://doi.org/10.1103/PhysRevLett.107.267002

60. M. F. Collins, G. G. Low, The magnetic moment distribution aroundtransition element impurities in iron and nickel, Proc. Phys. Soc., 86 (1965), 535. DOI: 10.1088/0370-1328/86/3/313

61. B. Drittler, N. Stefanou, S. Bl¨ugel, R. Zeller, P.H. Dederichs, Electronic structure and magnetic properties of dilute Fe alloys with transition-metal impurities, Phys. Rev. B, 40 (1989), 8203. DOI: https://doi.org/10.1103/PhysRevB.40.8203

62. E.A. Tereshina, D.I. Gorbunov, A.V. Andreev, K. Watanabe, Influence of Ru on Magnetism of R_2Fe_{17} (R = Y, Lu, and Er), IEEE Trans. Magn., 47 (2011), 3610. DOI: 10.1109/TMAG.2011.2146231

63. E.A. Tereshina, O. Isnard, A. Smekhova, A.V. Andreev, A. Rogalev, S. Khmelevskyi, Experimental and theoretical study of magnetic ordering and local atomic polarization in Ru-substituted Lu_2Fe_{17}, Phys. Rev. B, 89 (2014), 094420. DOI: 10.1103/PhysRevB.89.094420

64. S. Schönecker, M. Richter, K. Koepernik, H. Eschrig, Ferromagnetic elements by epitaxial growth: A density functional prediction, Phys. Rev. B, 85 (2012), 024407. DOI: https://doi.org/10.1103/PhysRevB.85.024407

65. D. Odkhuu, S.H. Rhim, N. Park, K. Nakamura, S.C. Hong, Jahn-Teller driven perpendicular magnetocrystalline anisotropy in metastable ruthenium Phys. Rev. B, 91 (2015), 014437. DOI: 10.1103/PhysRevB.91.014437

66. S. Boseggia, H.C. Walker, J. Vale, R. Springell, Z. Feng, R.S. Perry, M. Moretti Sala, H.M. Ronnow, S.P. Collins, D.F. McMorrow, Locking of iridium magnetic moments to the correlated rotation of oxygen octahedra in Sr_2IrO_4 revealed by x-ray resonant scattering, J. Phys.: Cond. Matt. 25(42) (2013), 422202. DOI: 10.1088/0953-8984/25/42/422202

67. S. Agrestini, K. Chen, C.-Y. Kuo, L. Zhao, H.-J. Lin, C.-T. Chen, A. Rogalev, P. Ohresser, T.-S. Chan, S.-C. Weng, G. Auffermann, A. Völzke, A. C. Komarek, K. Yamaura, M. W. Haverkort, Z. Hu, L. H. Tjeng, Nature of the magnetism of iridium in the double perovskite Sr_2CoIrO_6, Phys. Rev. B, 100 (2019), 014443. DOI: https://doi.org/10.1103/PhysRevB.100.014443

68. P. Alexeev, O. Leupold, I. Sergueev, M. Herlitschke, D.F. McMorrow, R.S. Perry, E.C. Hunter, R. Röhlsberger H.-Ch. Wille, Nuclear resonant scattering from ^{193}Ir as a probe of the electronic and magnetic properties of iridates, Scientific Reports 9 (2019), 5097. DOI: 10.1038/s41598-019-41130-3

69. D. Bessas, I. Sergueev, D. G. Merkel, A. I. Chumakov, R. Rüffer, A. Jafari, S. Kishimoto, J. A. Wolny, V. Schünemann, R. J. Needham, P. J. Sadler, and R. P. Hermann, Nuclear resonant scattering of synchrotron radiation by ^{187}Os, Phys. Rev. B 91 (2015), 224102. https://doi.org/10.1103/PhysRevB.91.224102

70. D. Bessas, D. G. Merkel, A.I. Chumakov, R. Rüffer, R. P. Hermann, I. Sergueev, A. Mahmoud, B. Klobes, M.A. McGuire, M.T. Sougrati, L. Stievano, Nuclear Forward Scattering of Synchrotron Radiation by ^{99}Ru, PRL 113(14) (2014), 147601. DOI: 10.1103/PhysRevLett.113.147601

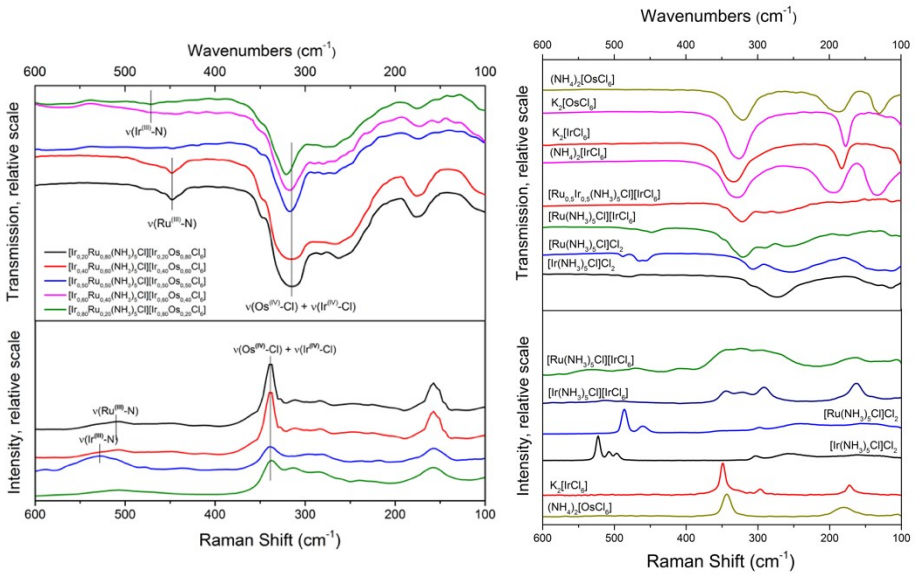

Figure 1. IR and Raman spectra of multimetallic coordination compounds (*left*) and some of their precursors (*right*).

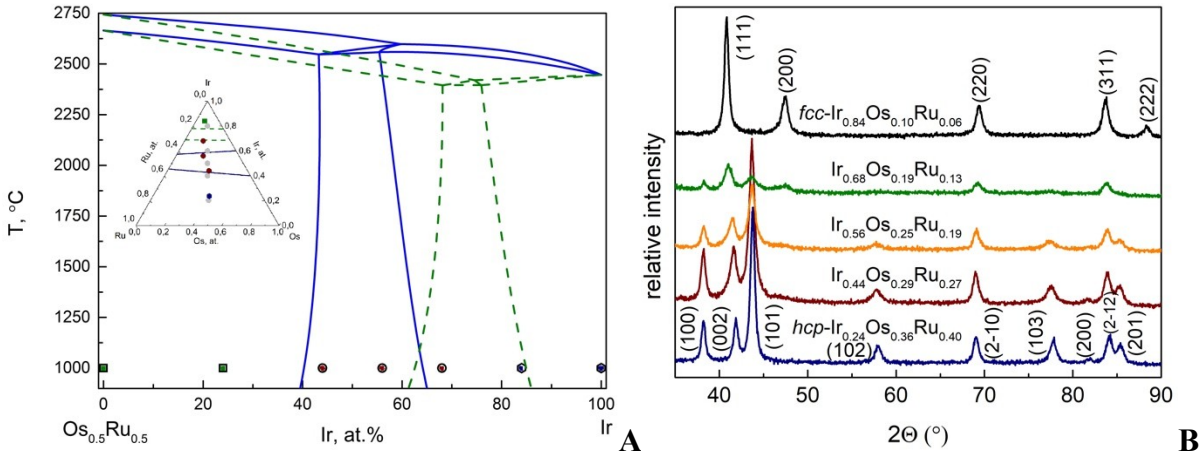

Figure 2. Compositions of prepared ternary alloys on the Ir–$Os_{0.5}Ru_{0.5}$ *quasi*-binary cross-section of the modelled ternary Ir–Os–Ru phase diagram (A*); solid line* corresponds to the sub-sub-regular model, *dashed line* corresponds to the ideal solutions model; *hexagons* represent *hcp*-structured single-phase alloys, *squares* – *fcc*-structured alloys, circles correspond to two-phase compositions and on the 2000 °C isotherm (*inset*). PXRD profiles of prepared ternary alloys (B, in house data, Cu*K*α-radiation).

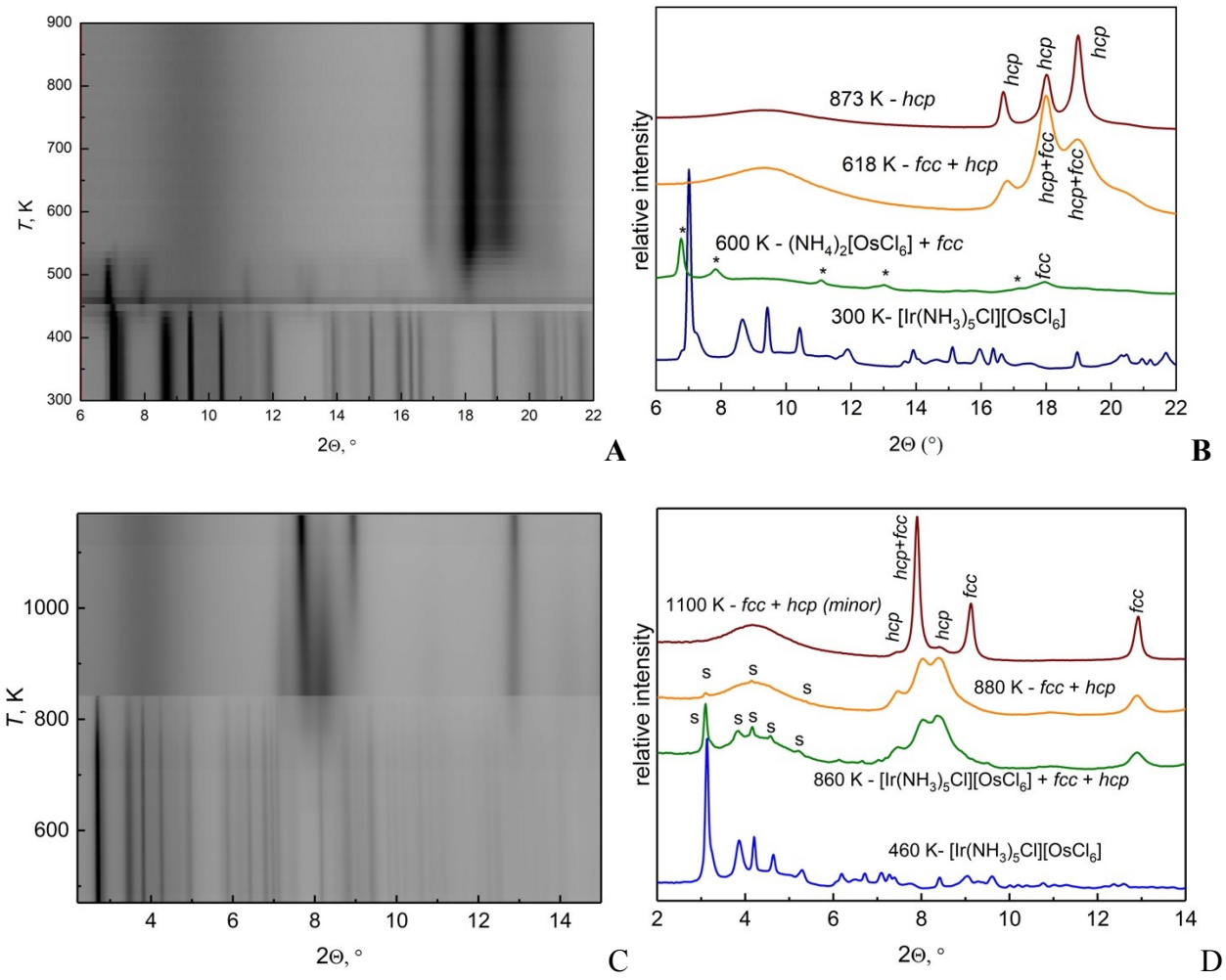

Figure 3. *In situ* PXRD data for $[Ir(NH_3)_5Cl][OsCl_6]$ heated in 5 vol.% H_2 / 95 vol.% He mixture (A and B; λ = 0.68894 Å) and in pure Ar flow (C and D; λ = 0.30860 Å). A and C correspond to temperature dependent data; B and D correspond to selected temperatures; s – diffraction lines for $[Ir(NH_3)_5Cl][OsCl_6]$, * – for $(NH_4)_2[OsCl_6]$.

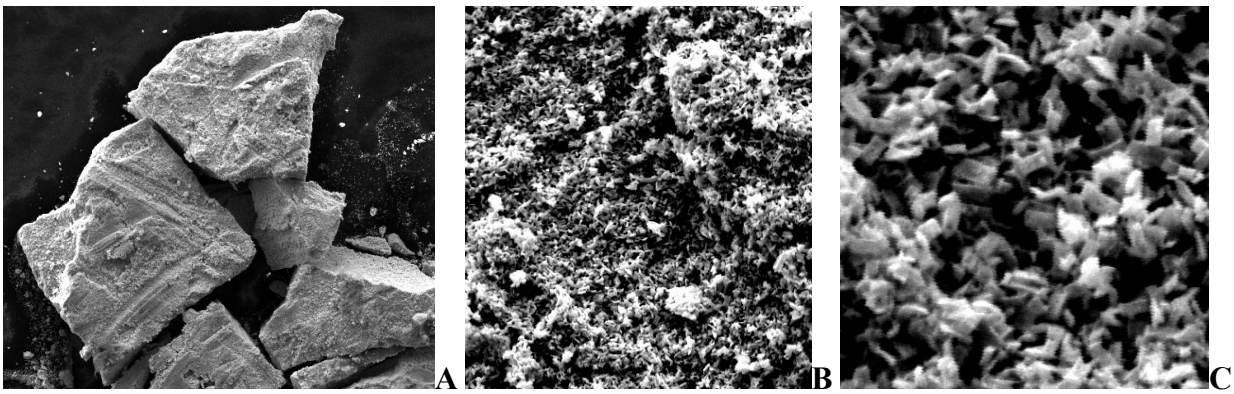

Figure 4. SEM images of two-phase $Ir_{0.44}Ru_{0.27}Os_{0.29}$. Horizontal full scale for A is 500 μm; B – 20μ, and C – 5μm.

.

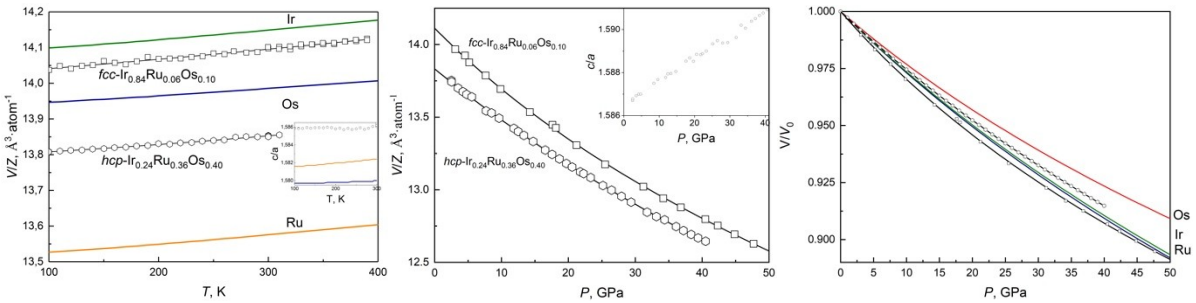

Figure 5. Thermal expansion curves for *hcp*–$Ir_{0.24}Ru_{0.36}Os_{0.40}$ (*hexagons*) and *fcc*–$Ir_{0.84}Ru_{0.06}Os_{0.10}$ (*squires*) in comparison with pure Ir, Os and Ru (*left*); room temperature pressure compressibility curves for *hcp*–$Ir_{0.24}Ru_{0.36}Os_{0.40}$ (*hexagons*) and *fcc*–$Ir_{0.84}Ru_{0.06}Os_{0.10}$ (*squares*) and pure metals (*solid lines*) in V/Z *vs.* P scale (*middle*); insets show temperature and pressure dependence of c/a values for *hcp*–$Ir_{0.24}Ru_{0.36}Os_{0.40}$; room temperature pressure compressibility curves for *hcp*–$Ir_{0.24}Ru_{0.36}Os_{0.40}$ (*hexagons*) and *fcc*–$Ir_{0.84}Ru_{0.06}Os_{0.10}$ (*squires*) and pure metals (*solid lines*) in V/V_0 *vs.* P scale (*right*).

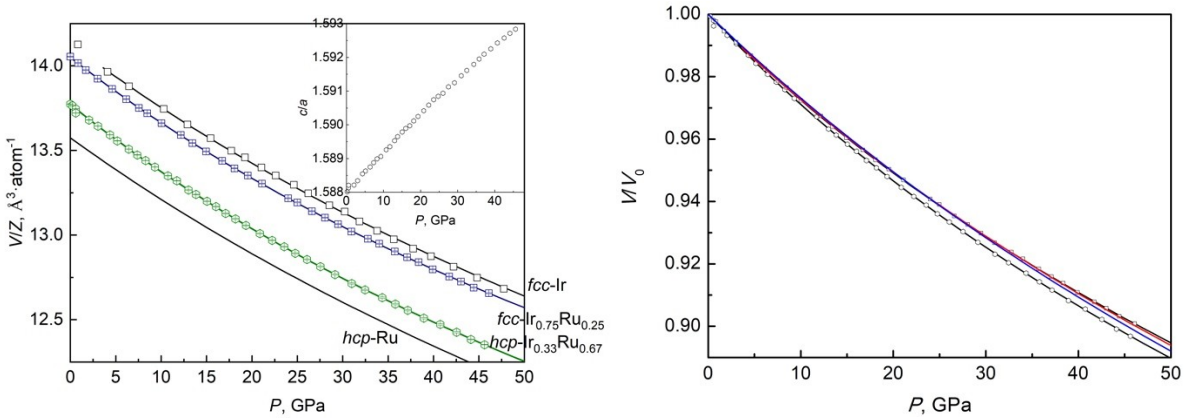

Figure 6. Room temperature pressure compressibility curves for *hcp*–$Ir_{0.33}Ru_{0.67}$ and *fcc*–$Ir_{0.75}Ru_{0.25}$ binary alloys and pure Ru and Ir metals in V/Z *vs.* P (*left*) and V/V_0 *vs.* P (*right*) scales (*inset* shows pressure dependence of c/a value for *hcp*–$Ir_{0.33}Ru_{0.67}$).

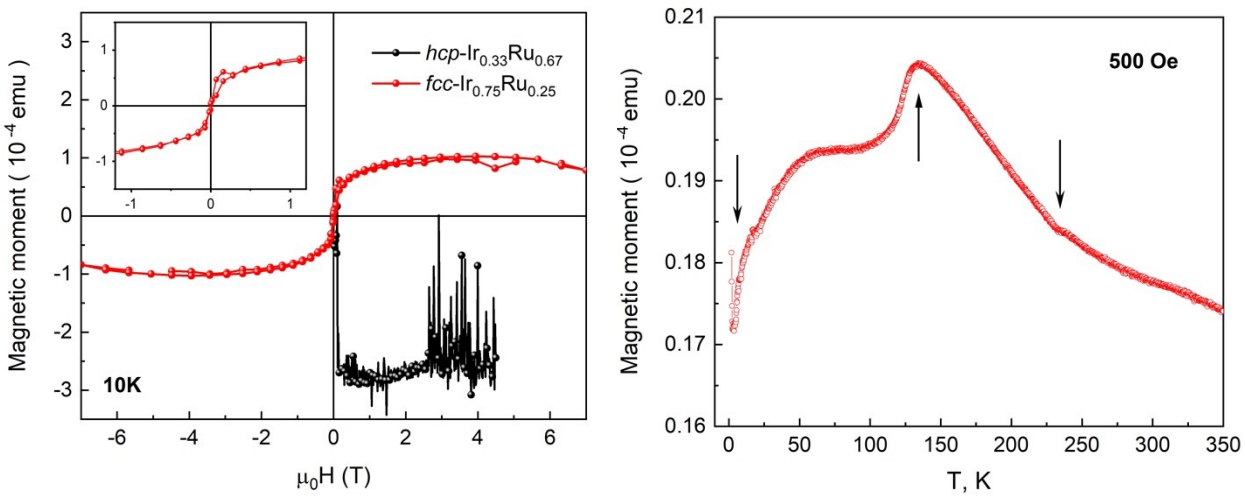

Figure 7. Field dependence of magnetic moment for *hcp*–$Ir_{0.33}Ru_{0.67}$ and magnetic hysteresis for *fcc*–$Ir_{0.75}Ru_{0.25}$ alloys measured at 10 K (*left*). Temperature dependence for *fcc*–$Ir_{0.75}Ru_{0.25}$ alloy recorded in the external magnetic field of 500 Oe (*right*). Vertical arrows on the right panel indicate the temperatures of possible magnetic phase transitions in *fcc*–$Ir_{0.75}Ru_{0.25}$.

Table 1. Phase composition of Ir–Ru binary and Ir–Os–Ru ternary alloys prepared from single-source precursors.

Nominal composition of single-source precursor	Analytical alloy's composition	a_{fcc}, Å	V/Z_{fcc}, Å^3·atom^{-1} (Z_{fcc} = 4)[c]	a_{hcp}, Å	c_{hcp}, Å	V/Z_{hcp}, Å^3·atom^{-1} (Z_{hcp} = 2)[c]	*fcc / hcp, wt.%*
$[Ir_{0.20}Ru_{0.80}(NH_3)_5Cl][Ir_{0.20}Os_{0.80}Cl_6]$	$Ir_{0.24(2)}Ru_{0.36(2)}Os_{0.40(2)}$[a]	—	—	2.721(2)	4.316(3)	13.832(2)	0 / 100
$[Ir_{0.40}Ru_{0.60}(NH_3)_5Cl][Ir_{0.40}Os_{0.60}Cl_6]$	$Ir_{0.44(2)}Ru_{0.27(2)}Os_{0.29(2)}$[a]	3.839(3)	14.149(2)	2.722(2)	4.339(3)	13.924(2)	10 / 90
$[Ir_{0.50}Ru_{0.50}(NH_3)_5Cl][Ir_{0.50}Os_{0.50}Cl_6]$	$Ir_{0.56(2)}Ru_{0.19(2)}Os_{0.25(2)}$[a]	3.774(3)	13.437(2)	2.719(2)	4.355(3)	13.941(2)	20 / 80
$[Ir_{0.60}Ru_{0.40}(NH_3)_5Cl][Ir_{0.60}Os_{0.40}Cl_6]$	$Ir_{0.68(2)}Ru_{0.13(2)}Os_{0.19(2)}$[a]	3.824(3)	13.985(2)	2.718(2)	4.363(3)	13.961(2)	27 / 73
$[Ir_{0.80}Ru_{0.20}(NH_3)_5Cl][Ir_{0.80}Os_{0.20}Cl_6]$	$Ir_{0.84(2)}Ru_{0.06(1)}Os_{0.10(1)}$[a]	3.832(3)	14.067(2)	—	—	—	100 / 0
$[Ru(NH_3)_5Cl]_2[IrCl_6]Cl_2$ [11]	$Ir_{0.33(1)}Ru_{0.67(1)}$[b]	—	—	2.716(2)	4.312(3)	13.770(2)	0 / 100
$[Ir_{0.50}Ru_{0.50}(NH_3)_5Cl][IrCl_6]$ [11]	$Ir_{0.75(1)}Ru_{0.25(1)}$[b]	3.727(3)	14.010(2)	—	—	—	100 / 0

[a] according to EDX.

[b] according to AAS.

[c] Atomic volumes for pure metals: V/Z_{fcc}(Ir) = 14.156(1) [36], V/Z_{hcp}(Os) = 13.9843(2) [34], V/Z_{hcp}(Ru) = 13.575(2) Å^3·atom^{-1} [38].

Table 2. Volumetric ambient pressure thermal expansion and room temperature compressibility of Ir–Ru, Ir–Os, and Ir–Os–Ru alloys.

Composition (max. P)	V_0/Z, Å^3·atom^{-1})[a]	$\alpha_0 \cdot 10^5$, K^{-1}	$\alpha_1 \cdot 10^9$, K^{-2}	V_0/Z, Å^3·atom^{-1} P = 1 bar)[b]	V_0/Z, Å^3·atom^{-1} According to Zen's rule	B_0, GPa B_0'	B_0, GPa According to Equation 1	Ref.
hcp–$Ir_{0.24}Ru_{0.36}Os_{0.40}$	13.832(1)	1.1(2)	2.7(5)	13.836(3)	13.876	362(4) 4.8(2)	—	Present study
(up to 41 GPa)								
fcc–$Ir_{0.84}Ru_{0.06}Os_{0.10}$	14.067(2)	0.55(1)	5(2)	14.111(4)	14.097	302(7) 6.4(5)	—	Present study
(up to 51 GPa)								
fcc–$Ir_{0.75}Ru_{0.25}$	—	—	—	14.050(1)	14.011	332(2) 5.4(1)	342.7	Present study
(up to 46 GPa)								
hcp–$Ir_{0.33}Ru_{0.67}$	—	—	—	13.773(1)	13.767	316(1) 5.1(1)	345.6	Present study
(up to 46 GPa)								
fcc–$Ir_{0.80}Os_{0.20}$	14.112(2)	1.3(1)	9(1)	14.09(1)	14.127	368(4) 4	354.2	[7]
(up to 20 GPa)								
hcp–$Ir_{0.55}Os_{0.45}$	14.092(2)	1.36(6)	4.8(9)	14.07(1)	14.090	395(5) 4	372.3	[7]
(up to 32 GPa)								
hcp–$Ir_{0.40}Os_{0.60}$	14.069(2)	—	—	14.06(2)	14.068	403(32) 4	384.3	[7]
(up to 20 GPa)								
hcp–$Ir_{0.20}Os_{0.80}$	13.982(4)	—	—	14.00(1)	14.039	420(5) 4	401.3	[7]
(up to 15 GPa)								
hcp–Os	13.9843(2)	1.35(1)	4.7(2)	14.01(1)	—	399(6) 4.04(4)	—	[34, 35]
(up to 500 GPa)								
fcc–Ir	14.156(1)	1.66(2)	7.3(3)	14.14(6)	—	341(10) 4.7(3)	—	[36, 37]
(up to 67 GPa)								
hcp–Ru	13.575(2)	1.57(2)	12.8(1)	13.575(2)	—	348(18) 3.3(8)	—	[38, 39]
(up to 56 GPa)								

[a] Atomic volume refined from PXRD data at ambient conditions.

[b] Atomic volume obtained from BM-EoS.